Microsc. Microanal. 19, 1558–1568, 2013
doi:10.1017/S1431927613013433

Microscopy AND Microanalysis

In Situ TEM Study of Catalytic Nanoparticle Reactions in Atmospheric Pressure Gas Environment

Huolin L. Xin,[1] Kaiyang Niu,[1] Daan Hein Alsem,[2] and Haimei Zheng[1,*]

[1]*Materials Sciences Division, Lawrence Berkeley National Laboratory, Berkeley, CA 94720, USA*
[2]*Hummingbird Scientific, Lacey, WA 98516, USA*

Abstract: The understanding of solid–gas interactions has been greatly advanced over the past decade on account of the availability of high-resolution transmission electron microscopes (TEMs) equipped with differentially pumped environmental cells. The operational pressures in these differentially pumped environmental TEM (DP-ETEM) instruments are generally limited up to 20 mbar. Yet, many industrial catalytic reactions are operated at pressures equal or higher than 1 bar—50 times higher than that in the DP-ETEM. This poses limitations for *in situ* study of gas reactions through ETEM and advances are needed to extend *in situ* TEM study of gas reactions to the higher pressure range. Here, we present a first series of experiments using a gas flow membrane cell TEM holder that allows a pressure up to 4 bar. The built-in membrane heaters enable reactions at a temperature of 95–400°C with flowing reactive gases. We demonstrate that, using a conventional thermionic TEM, 2 Å atomic fringes can be resolved with the presence of 1 bar O_2 gases in an environmental cell and we show real-time observation of the Kirkendall effect during oxidation of cobalt nanocatalysts.

Key words: environmental cells, gas flow, *in situ* TEM, environmental TEM, nanoscale reactions, Kirkendall effects

Introduction

In situ transmission electron microscopy (TEM) study of solid–gas interactions with high spatial resolution has been of particular interest in the study of chemical vapor deposition and heterogeneous catalysis (Hansen et al., 2002; Frances, 2010; Yoshida et al., 2012). TEMs are generally not compatible with a gaseous environment since a high vacuum environment needs to be maintained within the column to protect the electron emitter and to avoid beam-gas scattering and contamination. To perform *in situ* solid–gas experiments in a TEM, two viable routes have been developed—the differentially pumped system in the objective lens area (Boyes & Gai, 1997; Sharma & Weiss, 1998; Hansen & Wagner, 2012) and a closed environmental cell (E-cell; Creemer et al., 2008; de Jonge et al., 2010; Sun et al., 2011; Yaguchi et al., 2011; Allard et al., 2012; Yokosawa et al., 2012; Vendelbo et al., 2013). The differentially pumped system fills the entire objective lens area in the TEM column with low pressure gases. Differential pumping apertures allow the electron beam to go through while slowing the gases from escaping the objective area. The advantage of this system is that except for gas environments, no other physical objects interfere with the electron beam during imaging. Therefore, under a low gas pressure, high imaging sensitivity allows light-element materials, such as graphene, to be imaged with high resolution and contrast (Hansen & Wagner, 2012). For state-of-the-art commercial environmental TEMs (ETEMs), however, the pressure is limited to 20 mbar depending on the molecular weight of the gases (Sharma, 2001; Jinschek & Helveg, 2012). Another limitation is that the post-specimen differential pumping apertures block the high-angle scattered electrons. It limits annular dark-field scanning transmission electron microscopy (ADF-STEM) imaging to the low-angle regime. The low collection angles make the ADF-STEM images more subject to diffraction contrast.

Using a windowed gas flow cell approach, on the other hand, does not require any modifications to the TEM. Electrons do not need to travel through the gas with a long path, which is normally a few millimeters in commercial ETEM as defined by the pole piece gap. A windowed gas cell generally uses two silicon chips with micron size amorphous ceramic membranes. Their thicknesses are typically in the range of 25–50 nm for high electron transparency. However, because of the high fracture strength of these ceramic films (Chuang et al., 2004; Hatty et al., 2008), as well as the size of the viewing area that is needed, these cells can still withhold 1 bar or more of differential pressure. The gas path length in this system is controlled by the thin spacer between the two chips in the holder. It generally ranges from a few tens of nanometers to a few microns, which is three to five orders of magnitude smaller than that of the differentially pumped ETEM (DP-ETEM) (Creemer et al., 2008; de Jonge et al., 2010; Sun et al., 2011; Yaguchi et al., 2011; Allard et al., 2012; Yokosawa et al., 2012). With a bar of pressure, the gas path length of a few microns is equivalent to no more than a few nanometers of solid. Therefore, the limiting factor for resolution is not the gas pressure, but the membrane thickness (de Jonge et al., 2010). The advantages of using a windowed gas flow system is that it can be used in any TEM and the working pressure can be in the >1 bar regime. However, due to the mem-

Received May 11, 2013; accepted August 14, 2013
*Corresponding author. hmzheng@lbl.gov

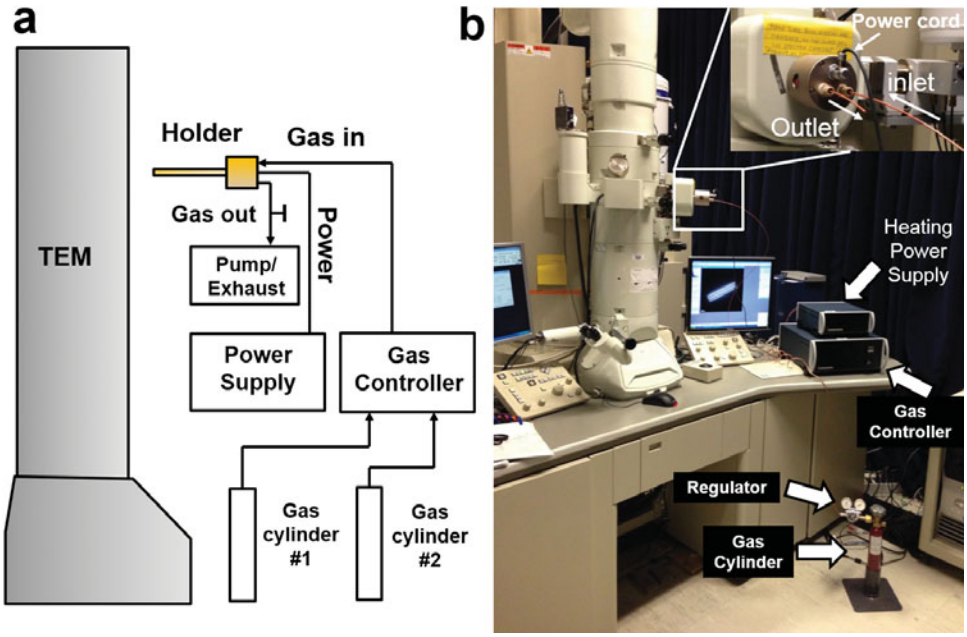

Figure 1. The gas flow holder system. **a**: Schematics of the gas flow holder system. **b**: Photograph of the system in the TEM laboratory.

brane windows, the imaging resolution and detection sensitivity are reduced compared to imaging TEM samples in vacuum.

Here, we present an *in situ* study of catalytic reactions with gas pressure of 1 bar, using a membrane-based cell environmental gas-flow heating holder. The on-chip membrane heaters enable *in situ* heating at 95–400°C in flowing reactive gases. We demonstrate that using conventional LaB_6 TEM instruments, atomic resolution can be preserved in this system with flowing gases and the dynamics of cobalt nanocatalysts due to the Kirkendall effect can be captured in real time.

Materials and Methods

Windowed Environmental Holder System

The *in situ* TEM gas holder system (Hummingbird Scientific, Lacey, WA, USA) includes a windowed gas flow cell with built-in electrical contacts, gas tubing connected to the cell allowing ~1 bar gases to flow through the cell while imaging, and a gas flow controller. Figure 1 shows a schematic of the system and a photograph of the setup in our lab. The flow system allows two gases to be mixed and fed to the holder inlet. As shown in Figure 1a, gases from the high pressure gas cylinders flow through pressure regulators into the gas controller box where the flow rate can be adjusted. When a positive differential pressure is established between the inlet and outlet, gases are injected through the inlet gas tubing into the gas cell and flow out from the outlet. The outlet of the holder can either be open to air or attached to a vacuum pump to allow regulation of pressure in the cell. More details on the gas environment control will be discussed in the following section.

Figure 2a shows a photograph of the flow holder. Gases flow into the guided channel through the chemical-resistant tubing. A three-point electrical connection is available at the end of the tip for on-chip heating (Fig. 2a, inset). The central components of this holder are the MEMS chips that form the sealed TEM gas cell (Fig. 2b). A gas flow cell is generally composed of two silicon chips—a chip with a spacer layer and a regular chip. These millimeter-size silicon chips contain windows with ~60 × ~200 μm in plane dimensions covered with electron transparent SiN_x membranes. After sample loading on the regular chip, the stack of two chips is placed in the holder tip and assembled into a gas cell using an O-ring sealing mechanism.

For heating experiments a heating chip replaces the regular chip. The heating element is placed on the electron transparent membrane. Before each experiment the sealed gas cell holder is pumped down in a dedicated vacuum check station to the same vacuum conditions as one would find in the TEM column at the specimen. This cautious step is a key to safe operation of windowed E-cell holders as it prevents any leaks of the system into the column—even small leaks can be detected this way. This is even more important for instruments with field emission guns where tip and ion getter pump longevity can be significantly compromised if pressure spikes and tip shutdowns occur frequently. Without this cautionary step, uptime of the TEM could be significantly compromised.

Gas Environment and Flow

The gas flow controller dynamically controls the required output pressure for a flow rate in the range of 0–0.5 sccm (standard cubic center meter/minute). The controller uses a thermal mass flow meter to measure gas volume flow. Two cylinders of gases were simultaneously used and their respective flow rate was controlled to mix the gases at any ratio. Even though premixed gases can often be ordered from gas vendors, this two-channel gas control system provides flexible adjustment of the gas ratio, allowing mechanistic studies of heterogeneous catalysis where gas composition can play an important role.

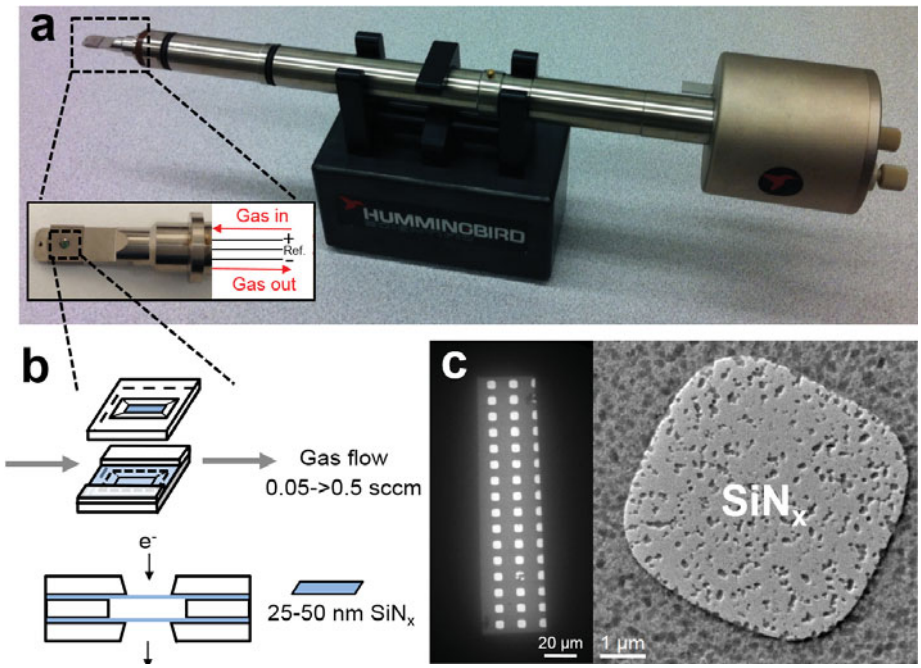

Figure 2. The design of the gas flow heating holder. **a**: The gas flow heating holder. **b**: The MEMS-type gas flow cell. **c**: The electron transparent windows of the membrane-type heating cell.

Using a high vacuum pump system on the outlet channel of the holder, the holder system can be purged rapidly and it can also be used as a below 1 bar pressure system. The pressure in the cell is expected to be equal to the regulator output pressure when the valve between the pump and the outlet is closed (Fig. 1). Using this system, we have stress tested the windowed gas cells with pressures up to 4.1 bar (59.7 psi or 4.06 atm)—the manufacturer's cell pressure differential rating is 1.3 bar—and have observed no damage to the SiN_x membranes and no detectable leakage in high vacuum.

As for the pressure distribution in the cell, if there is no gas flow and local heating is stabilized, the pressure in the cell is uniform after equilibration (Vendelbo et al., 2013). When the gas is flowing, a pressure gradient is built up along the tubing and the flow channel in the gas cell. Under the assumption of ideal gas, in steady state, the pressure gradient is given by Fick's law $p_oQ/ST_o = -D(dp/Tdx)$, where p_0 is the standard atmospheric pressure, Q is the flow rate in the dimension of standard unit volume per second, S is the cross-sectional area of the flow channel, T_0 is the standard room temperature, D is the diffusion coefficient of the gas, T is the temperature of the gas in the channel, and dp/dx is the change of pressure per unit length. At the boundary where two channels with different cross-sectional areas are connected, a sudden change of pressure would occur as determined by Bernoulli's equation. (Bernoulli's equation is applicable to compressible gas if the speed of the gas is sufficiently below the speed of sound.) Here, in this analysis, we assumed an ideal gas and neglected friction loss. The Darcy–Weisbach equation is a frequently used empirical equation for incompressible fluid, but modifications need to be made to it for gas calculations because both density and pressure are changing in gas flow (Smith et al., 2004; Accutech Co., n.d.; Crane Co., 2011). In addition, local heating would also cause a change of the pressure gradient profile. However, it is worth noting that in our gas cell the width of the observing window is only 60 μm in contrast to the 3 mm long flow channel. Typically, a flow rate of 0.2 sccm can be achieved with a differential pressure of 0.1 bar. Therefore, the pressure drop across the observation window is no more than ~2 mbar.

Heating

The temperature-dependent resistivity of the membrane heater decreases monotonically with temperature in the measured range (95–400°C). For calibration, the temperature of the heater has been measured by an IR camera while increasing applied current. The resistivity versus temperature dependency of the heater can then be built. (Calibrations were performed by the manufacturer on each batch of fabricated chips.) Because the effects of environment on temperature-dependent resistivity of the material are minimal, it is reasonably reliable to use the resistivity versus temperature relation (Creemer et al., 2008), rather than a current versus temperature relation to measure the temperature of the heating element. For example, with variable flow rate and different gases, the amount of heat that is carried away per unit time by the gas varies. Higher flow rate would require the heater to generate more heat to maintain the same temperature; therefore higher current is needed though the resistivity of the heater does not change. The resistivity model lines up within ±15°C in the 95–400°C temperature range.

Imaging Instrument

All imaging results were acquired in a thermionic JEOL 2100 with a high resolution pole piece (C_s = 1 mm) and a LaB_6 filament. A Gatan UltraScan 1000 CCD camera (Gatan, Pleasanton, CA, USA) was used for high-resolution imaging and a Gatan Orius CCD camera (Gatan) was used for high-throughput *in situ* imaging.

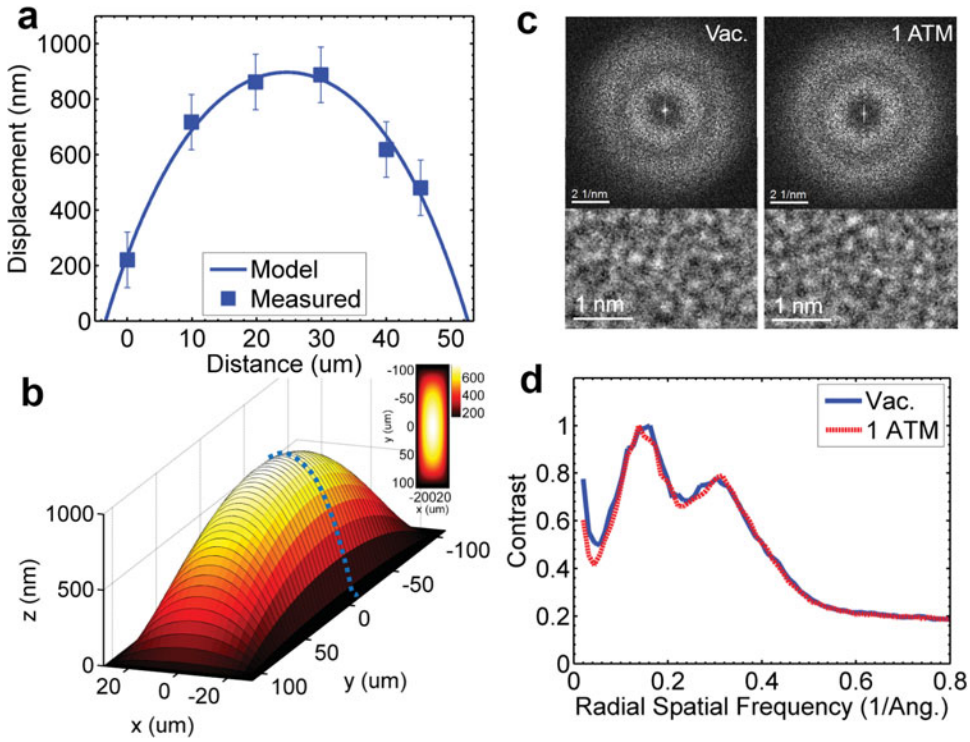

Figure 3. SiN_x window bulging and imaging resolution. **a**: The measured membrane bulging displacement. **b**: The calculated two-dimensional bulging profile of the window membrane. **c**: 2D fast Fourier transforms (FFTs) and images of the amorphous membrane with and without gas in the cell. **d**: The radially averaged contrast transfer profile of the 2D FFTs in (**c**).

Results

Imaging resolution and sensitivity are two of the most important parameters used to evaluate an ETEM. The advantage of a closed E-cell compared to a differentially pumped TEM around the objective aperture is its reduced gas path length that enables imaging with gas pressures three orders of magnitude higher. However, to withhold >1 bar of differential pressure, the ceramic membranes cannot be made arbitrarily thin. Other than the degradation due to the gas and the membranes, resolution is also limited by shot noise, thermal drift, and vibrations resulting from gas injection and pumping. Here, we evaluate the imaging performance of the E-cells under different environmental conditions (gas flow, pumping, heating, etc.) experimentally and theoretically. Finally, we will demonstrate nanoscale *in situ* reaction dynamics that can be achieved with this system by observing cobalt nanoparticles in oxygen gas at temperatures ranging from 150 to 350°C.

Gas Path Length and Bulging of Membrane Windows

The gas path length in a windowed E-cell is not entirely determined by the spacers that set the distance between the top and bottom MEMS chips. Due to the presence of differential pressure between the gas in the cell and the vacuum in the TEM column, the SiN_x membranes in the windows will bulge out under environmental conditions. This can greatly increase the gas path length.

The maximum displacement of the membrane is dependent on Young's modulus, Poisson ratio, thickness of the SiN_x membrane, window size, and the differential pressure (Vlassak & Nix, 1992). By increasing the thickness of the membrane or shrinking the size of the viewing window, the maximum bulging displacement at the center of the membrane can be reduced.

To characterize the bulging effect of the gas cells, we chose to use defocus in TEM mode to measure the distance between the top and bottom membrane. By monitoring the Thon ring diameter in the diffractogram of the amorphous membranes, we could achieve a measurement precision of ±10 nm. The accuracy of the defocus value given by the TEM software was confirmed by moving the membrane 10 μm out of focus through changing z height and defocusing the membrane back in focus. We found the displayed defocus value was the same as the z height change with <5% error. We have measured the distance between the top and bottom membranes across the width of the membrane at six locations under static atmospheric condition (inlet and outlet to the cell are open to air) and under near-vacuum condition (inlet sealed and outlet pumped by the vacuum pump down to $\sim 10^{-6}$ mbar). The single side bulging displacement is the distance difference between the two conditions divided by two. Figure 3a shows the measured bulging displacement of a single side of a membrane across the width of the window. We found that with a window width of 60 μm, the membrane can bulge out nearly 1 μm. This means that in the center of the viewing window, an additional 2 μm need to be added to the gas path length in addition to the spacer thickness.

The deflection of a membrane under a uniform pressure can be described by a theoretical model (Vlassak & Nix, 1992):

$$w = w_0 \frac{1}{a^2 b^2}(a^2 - x^2)(b^2 - y^2)\left[1 + \frac{R}{a^2}x^2 + \frac{R}{b^2}y^2\right], \quad (1)$$

where a and b are the half width and half length of the window; w_0 is the maximum bulging displacement; and R is a dimensionless geometric parameter. By fitting this equation with $y = 0$ to the measured displacement in Figure 3a, the unknown parameters—w_0 and R—can be determined.

Figure 3b plots the two-dimensional bulging of the membrane. It shows the change of displacement is relatively gradual at the corners and the shorter edges. Imaging should be preferentially performed in these areas. It is worth noting that the effect of window bowing is especially important to liquid cell experiments (de Jonge & Ross, 2011) but not as much in gas cell experiments because the density of atmospheric gas is three orders of magnitude lower than that of water—to first order, gas with a thickness of 1 μm is equivalent to 1 nm of solid/liquid materials in scattering electrons. (Please note that a subtlety in defining the solid equivalent thickness of gas resides in the difference in evaluation of this value. This value can be measured by total scattering probability or by broadening of the electron beam in real space. Scattering probability is strictly proportional to the thickness, however, broadening of the electron beam is proportional to 3/2 power of the thickness. In this article, we use the total scattering probability to estimate solid equivalent thickness.) In the next section we will focus in more detail on how gas path length and the membrane thickness limit resolution.

TEM Imaging Resolution in a Gas Cell

We first show how information transfer of amorphous membranes changes with gas in the cell. Images of the SiN_x membrane (df ~ 95 nm; measured by defocusing from the Gaussian focal plane) with and without gas in the E-cell are shown in Figure 3c. There are no perceivable differences in the images and the 2D fast Fourier transform (FFT) and it is quantitatively confirmed by comparing the radially averaged FFT of the two images. Figure 3d shows the information transfer with and without changes in the atmosphere. Again this is due to the fact that a micron thick gas is the first-order equivalent to 1 nm of solid/liquid materials. The ~2 μm gas path length results in ignorable degradation of resolution in our thermionic instrument.

In conventional TEM, imaging resolution of supported materials is degraded through elastic and chromatic blurring. Elastic blurring is due to multiple scattering of electrons that causes a point spread in real space. It is sample dependent and is subject to the top–bottom effect. Chromatic blurring, however, is both sample and instrument dependent. In first-order approximation, it is not subject to the top–bottom effect. Below we have theoretically studied elastic blurring, chromatic blurring, and the top–bottom effect in the context of E-cells.

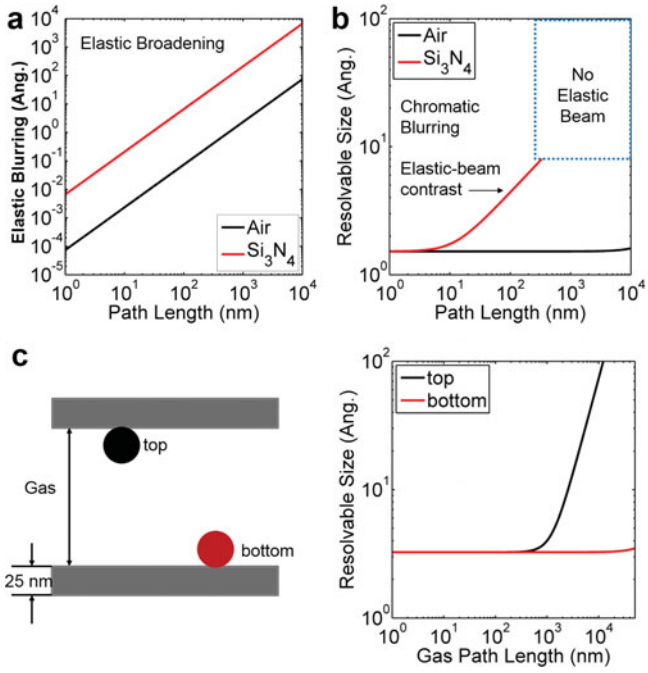

Figure 4. Reduction of imaging resolution in closed environmental gas cells. **a**: Comparison of resolution degradation due to elastic broadening in air and in silicon nitride. **b**: Comparison of resolution degradation due to inelastic broadening in air and in silicon nitride. **c**: TEM top-and-bottom effect in a closed gas cell.

Elastic Blurring

In first-order approximation, elastic blurring is due to point spreading of the electron exit waves of the objects of interest. It is well known that beam spreading follows a $t^{3/2}$ power law (Reed, 1982; Rez, 1983; Goldstein et al., 2003). The elastic blurring effect can be formulated as

$$\text{In gases} \qquad b = 364 \frac{\bar{Z}}{E_0}\left(\frac{p}{T}\right)^{1/2} t^{3/2}, \quad (2)$$

$$\text{In solid materials} \qquad b = 364 \frac{\bar{Z}}{E_0}\left(\frac{\rho}{\bar{A}} N_0 k_0\right)^{1/2} t^{3/2}, \quad (3)$$

where b is point broadening in meters, $\bar{Z}$ is the average atomic number, E_0 is the incident beam energy in eV, p is pressure in Pascal, T is temperature in Kelvin, t is thickness in meters, ρ is density in g/m^3, $\bar{A}$ is average atomic weight in g/mol, N_0 is Avogadro number, and k_0 is Boltzmann constant.

Figure 4a shows the resolution degradation due to elastic broadening as a function of thickness for air and Si_3N_4, respectively. It shows that in order to produce a blurring width of 1.5 Å, the path lengths needed for Si_3N_4 and air are 37 and 744 nm, respectively. It is worth noting that these numbers are pessimistic estimates, especially if the path length is smaller than two times the elastic mean free path.

Chromatic Blurring

Chromatic blurring is due to the energy spread of the incident beam and inelastic energy loss in the sample. Therefore, this effect is dependent on the instrument and the

sample. In an instrument with a LaB_6 filament, the energy spread of the incident electron is ~1.5 eV. It provides a rather significant information damping through the temporal coherent envelope. The envelop can be calculated through $\exp[-\frac{1}{2}\pi^2\lambda^2 C_c^2(\Delta E_{\mathrm{FWHM}}/2\ln(2)E_0)^2k^4]$, where ΔE_{FWHM} is the full-width at half maximum energy spread of the incident beam, E_0 is the incident electron energy, and C_c is the chromatic aberration coefficient, λ is incident electron wavelength, and k is the transverse spatial frequency. Assuming $\Delta E_{\mathrm{FWHM}} = 1.5$ eV, $C_c = 1.4$ mm, and $E_0 = 200$ keV, the information limit with 1/10 temporal coherent envelope contrast criterion is 1/1.52 $Å^{-1}$ in a 200 keV, $C_s = 1.0$ mm instrument. (Here we assume information transfer is limited by inelastic scattering but not convergence of illumination.)

The second component of chromatic blurring is due to inelastic scattering. Among all the inelastic scattering events, low energy loss (low-loss) signals dominate the total inelastic scattering cross section. Because low-loss signals preserve the coherent elastic contrast, to the first-order approximation, chromatic blurring does not have a top–bottom effect.

The mean energy loss as a function of thickness characterizes the broadening of the electron in the energy domain. It effectively lowers the limit of information transfer through damping the temporal coherent envelope $[d_c \sim ((\Delta E/E_0)\lambda C_c)^{1/2}]$ (Carter & Williams, 2009). The coherent treatment of inelastic scattering-induced blurring is debatable especially when the thickness of the substrate is larger than two times the inelastic mean free path where nearly all electrons have been scattered out of the zero-loss beam. In this regime, it is more suitable to use the incoherent formula, i.e., $(d_c = (\Delta E/E_0)C_c\alpha_{\max})$ (Carter & Williams, 2009). In the following, we only consider coherent treatment to give an optimistic estimate of elastic-beam resolution.

The mean energy loss ΔE as a function of thickness is an important relation for the calculation of chromatic blurring. Here we prove that it increases linearly with thickness. Let us assign that thickness as t and inelastic mean free path as λ. Because inelastic scattering is a Poisson process, the probability of finding an electron in an n^{th} plasmon-loss event is (Egerton, 2011)

$$p_n = \frac{1}{n!}\left(\frac{t}{\lambda}\right)^n \exp\left(-\frac{t}{\lambda}\right). \tag{4}$$

For simplicity, here we assume the mean energy loss of single-scattering events is approximately equal to the Plasmon energy E_p. Then the mean energy loss as a function of thickness is

$$\begin{aligned}\overline{\Delta E}_{in} &= \sum_{n=1}^{\infty} nE_p p_n = E_p \sum_{n=1}^{\infty} n\frac{1}{n!}\left(\frac{t}{\lambda}\right)^n \exp\left(-\frac{t}{\lambda}\right)\\ &= E_p \frac{t}{\lambda}\exp\left(-\frac{t}{\lambda}\right)\sum_{n=1}^{\infty}\frac{1}{(n-1)!}\left(\frac{t}{\lambda}\right)^{n-1}\\ &= E_p \frac{t}{\lambda}\exp\left(-\frac{t}{\lambda}\right)\exp\left(+\frac{t}{\lambda}\right) = E_p\frac{t}{\lambda}.\end{aligned} \tag{5}$$

Then the total energy broadening is an addition of the two components in quadrature, that is,

$$\overline{\Delta E}(t) = \sqrt{\Delta E_0^2 + \overline{\Delta E}_{\mathrm{in}}(t)^2}. \tag{6}$$

Figure 4b plots the comparison between chromatic blurring of Si_3N_4 and air as a function of path length. Here the resolvable size is determined by the 1/10 contrast criterion. It clearly shows that for a LaB_6 instrument, gas would not result in noticeable chromatic blurring until the gas path length approaches 1 μm. In contrast to the elastic blurring effect, the chromatic effect of gas starts to degrade resolution at a much larger path length because it scales linearly with thickness while elastic blurring scales with $t^{3/2}$.

Top–Bottom Effect

In conventional TEM, the object of interest is preferred to be located at the exit surface. By doing so, elastic blurring of the object's exit wave is minimized. To illustrate this aspect for the E-cell, we plot the top–bottom effect in Figure 4c. Here the membranes are set to be 25 nm thick with gas path length as an adjustable variable. The difference in resolution between the top and bottom surfaces is dramatic. Due to the elastic blurring's fast scaling with thickness ($t^{1/2}$), the resolution degradation becomes noticeable when the gas path length approaches 1 μm; however, for objects attached to the bottom membrane, the effect only becomes noticeable when the gas path length reaches 40 μm.

Comparison with DF-ETEM

To identify how to improve imaging resolution using windowed E-cells and DP-ETEM, it is worth comparing the theoretical phase-contrast imaging performance of a windowed E-cell to that of a DF-ETEM. We assume the windowed E-cells are using 25-nm-thick SiN_x membranes and the samples are attached to the bottom membranes to optimize high-resolution TEM (HRTEM) resolution. Table 1 lists the calculated HRTEM point resolution of DF-TEM and windowed E-cells under combinations of multiple different types of operating conditions (e.g., lens aberrations, electron emitters, pressures, and electron gas path lengths). Lens aberration (C_s's and C_c's) conditions of four popular commercial TEMs are considered. The dependence on thermionic emitters (LaB_6, energy FWHM = 1.5 eV) and Schottky field emitters (S-FEG, energy FWHM = 0.45 eV) are also included. Here the incident beam energy and the convergence angles are set to be 200 keV and 0.5 mrad for a unified comparison. (A beam convergence angle of 0.5 mrad is slightly small for LaB_6 emitters due to the low brightness. However, with thermally settled samples, this condition can provide improved imaging resolution especially for thin samples.)

First, focusing on trends for the windowed E-cells in Table 1 (three columns from the right), it is found that the resolution is less dependent on C_s but more on C_c. As shown in Supplementary Figures 4a, 4b, and 4c, the combined information transfer envelope is dominated by the temporal-coherence envelope. Because the temporal coherence envelope—$\exp[-\frac{1}{2}\pi^2\lambda^2C_c^2(\Delta E_{\mathrm{FWHM}}/2\ln(2)E_0)^2k^4]$—is independent of C_s, the E-cell imaging resolution is primarily

Table 1. Comparison of HRTEM Point Resolution between DF-ETEM and Windowed Environmental Cells (E-Cells) Under Their Respective Operating Conditions.*

		DP-ETEM									Windowed E-Cells (2×25 nm SiN_x wins)		
		Pressurized Electron Path Length/Pole Piece Gap (mm)									Gap (μm)		
		2			5.4			11			0.5	2	20
200 kV ($\beta_{max} = 0.5$ mrad)		Air Gas Pressure (mbar)											
		0.1	1	10	0.1	1	10	0.1	1	10	1000		
C_s/C_c (mm)	Type	Resolvable Feature Size under 1/10 Contrast Criterion (Å)											
3.4/3.1	S-FEG	3.3	3.3	3.4	3.3	3.3	4.2	3.3	3.3	5.5	5.0	5.0	5.0
	LaB_6	3.4	3.4	3.6	3.4	3.4	4.3	3.4	3.5	5.5	5.0	5.0	5.1
1.2/2.0	S-FEG	2.3	2.3	2.4	2.3	2.3	3.2	2.3	2.3	4.4	3.9	3.9	4.0
	LaB_6	2.4	2.4	2.6	2.4	2.4	3.3	2.4	2.5	4.4	4.0	4.0	4.0
1.0/1.4	S-FEG	2.1	2.1	2.2	2.1	2.1	2.7	2.1	2.1	3.7	3.4	3.4	3.4
	LaB_6	2.2	2.2	2.3	2.2	2.2	2.8	2.2	2.2	3.7	3.4	3.4	3.4
0.5/1.1	S-FEG	1.7	1.7	1.8	1.7	1.7	2.4	1.7	1.7	3.2	3.0	3.0	3.0
	LaB_6	1.8	1.8	1.9	1.8	1.8	2.4	1.8	1.8	3.3	3.0	3.0	3.0
0.1/2.0	S-FEG	1.1	1.1	1.9	1.1	1.2	3.0	1.1	1.5	4.3	3.8	3.8	3.9
	LaB_6	1.8	1.8	2.2	1.8	1.9	3.1	1.8	2.0	4.3	3.9	3.9	3.9

*For windowed cells, samples are assumed to be attached to the bottom membranes. Here, the given values reflect point resolution of imaging weak phase materials with 1/10-contrast ratio criterion. Lattice spacings of heavy element containing crystals smaller than the specified values, however, can be resolved under strong diffracting conditions due to improved signal-to-noise ratio and amplification of nonlinear terms. Two commercially available DF-TEM settings are shaded with gray background color. It is worth noting that latest commercial models (e.g., Environmental Titan) are generally operated at 300 or 80 kV. The below table provides a demonstration of trends rather than accurate numbers for all acceleration voltages.

limited by the use of the thick (50 nm combined) SiN_x window that provides an energy spread of ~6.25 eV. It is worth noting that even though the values in Table 1 indicate that S-FEG only improves resolution marginally, practically the ~10× brightness improvement of S-FEG over LaB_6 provides ~3× improvement in signal-to-noise ratio, this could allow information with 1/20 to 1/30 contrast ratio to be resolved in imaging.

Supplementary Material

To view Supplementary Figures 1–5 and Supplementary Movies 1 and 2 for this article, please visit http://dx.doi.org/10.1017/S1431927613013433.

Compared with windowed E-cells, DP-ETEM has significantly higher imaging resolution under ≤10 mbar gas pressures except for the case of the 11 mm pole piece gap. As shown in Supplementary Figures 4c and 4e, if samples are thin enough, aberration-uncorrected DF-ETEMs are not limited by chromatic blurring but partial spatial coherence resulted from unparalleled illumination—a 0.5 mrad beam convergence angle is assumed. Different from the windowed E-cells, correction of C_s can significantly improve spatial resolution due to the reduction of information damping through the spatial coherence envelope (Supplementary Fig. 4d versus 4e). As shown in Supplementary Figure 4e, when C_s is reduced to 0.1 mm or below, information transfer is limited by chromatic blurring. The energy spread due to inelastic loss in the gas is 0.04, 0.4, and 4.0 eV, respectively. This suggests that a monochromator can improve HRTEM resolution in the 0.1 mbar region; however, a post-specimen C_c corrector is needed to significantly improve information transfer at 1 mbar and above (Haider et al., 2008; Kisielowski et al., 2008).

In summary, HRTEM imaging in windowed E-cells is primarily limited by chromatic blurring resulting from the membrane windows. In uncorrected field-emission DP-ETEMs, HRTEM resolution can be more affected by beam convergence. However, in aberration-corrected field-emission DP-ETEMs, chromatic aberration is the dominant limiting factor. C_c correction can significantly improve imaging resolution for both windowed E-cells and corrected/uncorrected DP-ETEMs in all pressure regimes (Haider et al., 2008; Kisielowski et al., 2008); a monochromator, however, is only notably useful in the sub-mbar regime for corrected DP-ETEMs.

Imaging in Realistic Environmental Conditions

As shown in Table 1, our system should, in principle, provide ~3 Å resolution for imaging of nanoparticles in the gas flow cell. However, if gas tubing were attached to the holder

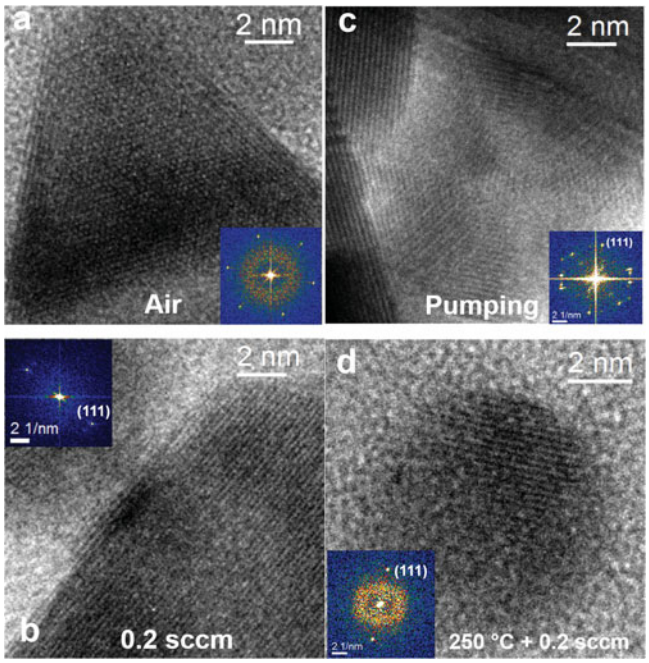

Figure 5. Imaging of (**a–c**) Pd and (**d**) Pt particles loaded in the gas cell in (**a**) atmospheric air (no flow), in (**b**) flowing oxygen at 0.2 sccm, at (**c**) full speed pumping, and at (**d**) 250°C with flowing oxygen at 0.2 sccm.

and especially if the pump is operating, coupled vibrations could limit information transfer. Here, to test our system in realistic conditions, we have imaged 8–15 nm Pd and Pt nanoparticles under four gas conditions: (1) atmospheric condition (inlet and outlet are open to the lab atmosphere), (2) flowing oxygen gas at 0.2 sccm (~1.1 bar in the cell), (3) full speed pumping on the outlet with the inlet open to air (~0.5 bar in the cell), and (4) we also imaged the nanoparticles with heating at 250°C and flowing oxygen gas at 0.2 sccm (~1.1 bar in the cell). Figure 5 demonstrates images of Pd/Pt nanoparticles in the gas cell obtained at the specified conditions, respectively. The images show that the ~2.2 Å Pd/Pt (111) lattice planes can be resolved even when the system is under flowing and heating conditions. Beyond 2 Å, information in the gas cell was also obtainable (Supplementary Fig. 1). This shows the high-resolution imaging capabilities of the TEM windowed gas cell flow system. It is worth noting that imaging tests using Pt/Pd nanocrystals show a resolution significantly better than our theoretical evaluation. Our theoretical prediction uses a linear imaging model which is only applicable to imaging weak phase materials. However, under strong diffraction conditions in aligned heavy atom matrices, both the nonlinear and linear interaction can be important (Van Aert et al., 2010).

Real-Time Observation of Reaction of Cobalt Nanoparticles

In situ observation of chemical reactions is essential for revealing spatially resolved reaction pathways. However, many reactions, such as bulk oxidation of 3*d* transition metals (Yin et al., 2004; Chenna et al., 2011), do not rapidly occur at room temperature. The membrane-type heating chip provides a temperature controllable reaction platform with flowing reactive gases. To demonstrate the *in situ* heating capability under environmental conditions, we operated oxidation reactions of cobalt nanoparticles in the gas cell with flowing oxygen (0.2 sccm) while ramping temperature from 150 to 250°C and 250 to 350°C at ~5°C/s.

Supplementary Movie 1 shows the oxidation trajectory of the cobalt nanoparticles (150–250°C). The images were aligned to remove the drift due to membrane expansion. From the alignment, drift rate can be extracted. Figure 6a shows the time-dependent drift rate as a function of time. The maximum drift rate was 2.9 nm/s after 100°C increase in temperature. After reaching its maximum, drift rate decreased exponentially. The time constant was ~75 s (the time it takes to drop to 36.8% of the maximum speed). The relatively slow drift, and the short settling time constant with relatively fast temperature ramping are attributed to the membrane-type heater design. It provides *in situ* tracking and imaging capabilities improved over traditional furnace-type heating holders (see Supplementary Fig. 2 for drift performance of conventional heating holder). Additionally, we performed site-dependent drift measurements under heating from 150 to 350°C (Figs. 6c, 6d). We chose one corner site, one edge site by the shorter side of the window, one edge site by the longer side of the window, and a center site. The measured drift trajectories shows trends that are expected from the expansion of a membrane with an expansion center slightly lower to site 3. Regardless of the expansion trajectory, this study shows it is preferable to choose edge and corner sites for *in situ* imaging because they have lower peak drift rates (Fig. 6d).

Figure 7a shows the time-lapse still images of three selected Co particles. Figures 7a(I) and 7a(II) visualize the shrinkage of the metallic cobalt core in close to cross-section view. They demonstrate the core can shrink with a unidirectional retraction front [Fig. 7a(I)] and a sweeping retraction front [Fig. 7a(II)]. Figure 7a(III) shows the shrinkage of the metallic core in projection view—the retraction front's normal direction is close to the beam incident direction. The images show the projection images of the metallic core when the shell is less than half filled. In projection, the residual metallic puddle is faceted, which is likely shaped by the faceted hollow shell.

Figure 7d shows quantification of the volume trajectory of the metallic core in Figure 7a(I). It shows that the metallic core volume started to rapidly decrease when temperature reached 250°C. After the first volume decreasing phase, volume shrinkage dwelled for a short period to time at the first plateau (① in Fig. 7b). Then a second rapid decreasing phase initiated, but the volume shrinkage rate was much lower than that of the first phase. After a second shrinkage stagnation plateau (② in Fig. 6b), the metallic core was finally eliminated, but at an even slower volume shrinking rate. This shrinkage stagnation phenomenon in the Kirkendall effect (Yin et al., 2004; Railsback et al., 2010) is likely related to the particle's unisotropic boundary con-

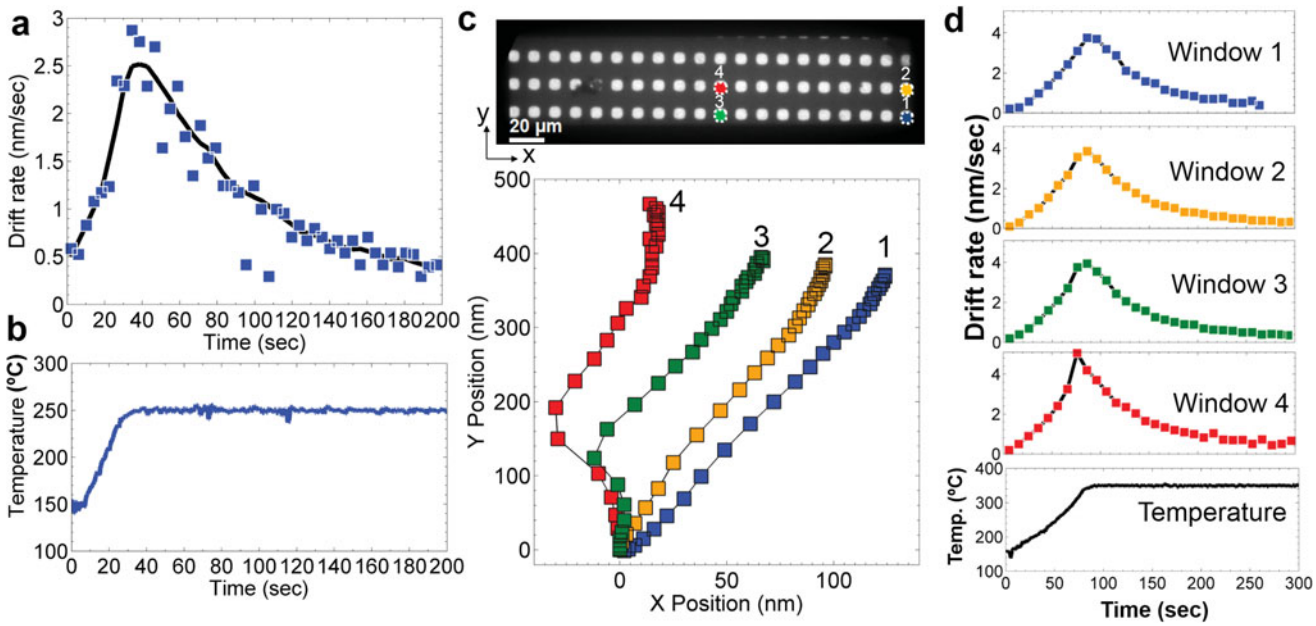

Figure 6. Characterization of thermal drift rate of the membrane heater. **a**: Drift rate measured using Supplementary Movie 1 with heating from 150 to 250°C. **c–d**: Site-dependent drift measurement under heating from 150 to 350°C. **c**: The movement trajectories of objects on four label windows. Time intervals between two adjacent measurement points are 10 s. **d**: Measured drift rate of the four sites as a function of time.

ditions. As shown in Figure 7a(I), the particle's oxide shell is in contact with other particles with upper and lower right boundaries open.

Moreover, with the kinetic data (Fig. 7d) we can estimate the diffusion coefficient of cobalt in the cobalt oxide shell at 250°C. According to Fick's law, the diffusion flux of cobalt in the oxide shell is approximately $J = D((\rho - 0)/\bar{d})$, where D is the diffusion coefficient, ρ is the density of cobalt, and $\bar{d}$ is the average oxide shell thickness (see Supplementary Fig. 4 for derivation). Here we assume surface diffusion of cobalt on cobalt oxide is must faster than cobalt diffusion in the cobalt oxide shell; then the diffusion cross section can be approximated as the inner surface area of the shell, that is, $S = 4\pi r^2$, where r is the inner radius of the shell. For the metallic core volume to decrease to half of its initial volume, the time—$t_{1/2}$—required is $t_{1/2} = (\frac{1}{2} \times \frac{4}{3}\pi r^3\rho)JS = (\frac{1}{2} \times \frac{4}{3}\pi r^3\rho)/((D\rho/\bar{d}) \times 4\pi r^2) = \frac{1}{6} \times r\bar{d}/D$. From Figure 7d, $t_{1/2}$ is estimated to be 19 s. (Estimated from Fig. 7, $r = 6.3$ nm and $\bar{d} = 5$ nm.) Therefore, we can derive the diffusion coefficient to be $D = 0.28$ nm^2/s $= 0.28 \times 10^{-14}$ cm^2/s. The most significant source of systematic errors in our calculation is the estimate of the diffusion cross-section S; nonetheless, using the shell inner surface area should be correct within the order of magnitude. Therefore, taking account of systematic errors, the confidence interval of our calculated diffusion coefficient is (0.28×10^{-14} to 2.8×10^{-14} cm^2/s). Our diffusion coefficient is four to five orders of magnitude larger than the bulk self-diffusion coefficient of Co in CoO reported in previous studies—$D = 4.36 \times 10^{-19}$ cm^2/s at 250°C (Chen et al., 1969). By investigating the as-prepared cobalt nanoparticles in aberration-corrected STEM, we found that the initial oxide shell is composed of polycrystalline cobalt oxides with nanoscale grain sizes (Supplementary Fig. 3). Therefore, it is highly likely in our experiment that cobalt diffusion through the oxide shell is dominated by grain boundary diffusion, which is typically multiple orders of magnitude faster than bulk diffusion in 3*d* transition metal oxides (Atkinson, 1986).

According to theoretical calculations (Gusak et al., 2005), hollow nanoparticles are thermodynamically unstable; they tend to collapse into solid particles because a solid particle has a lower surface energy than a hollow sphere. To provide an *in situ* study of the structural stability of the hollow oxide nanoparticles, we stress tested the same nanoparticles shown in Supplementary Movie 1 with the same oxygen flowing condition (0.2 sccm) by increasing the heating temperature from 250 to 350°C. Supplementary Movie 2 shows real-time imaging of cobalt oxide nanoparticles. A majority of hollow nanoparticles underwent a significant restructuring in agreement with theoretical predictions—the shell collapsed and the hollow core was filled (Fig. 7c). During the collapsing event, a large portion of particles showed significant changes in diffraction contrast. This suggest that reorientation and merging of the small polycrystalline grains occurred at 350°C, which, on the other hand, were not kinetically activated at the previous shell forming temperature—250°C.

This *in situ* study reveals a diffusion pathway in the Kirkendall effect and the instability of the hollow oxide structure (TOC figure). The technique is not limited to oxidation of nanoparticles, and it can be applied to many other nanocatalysts where reaction-driven shape changes are important.

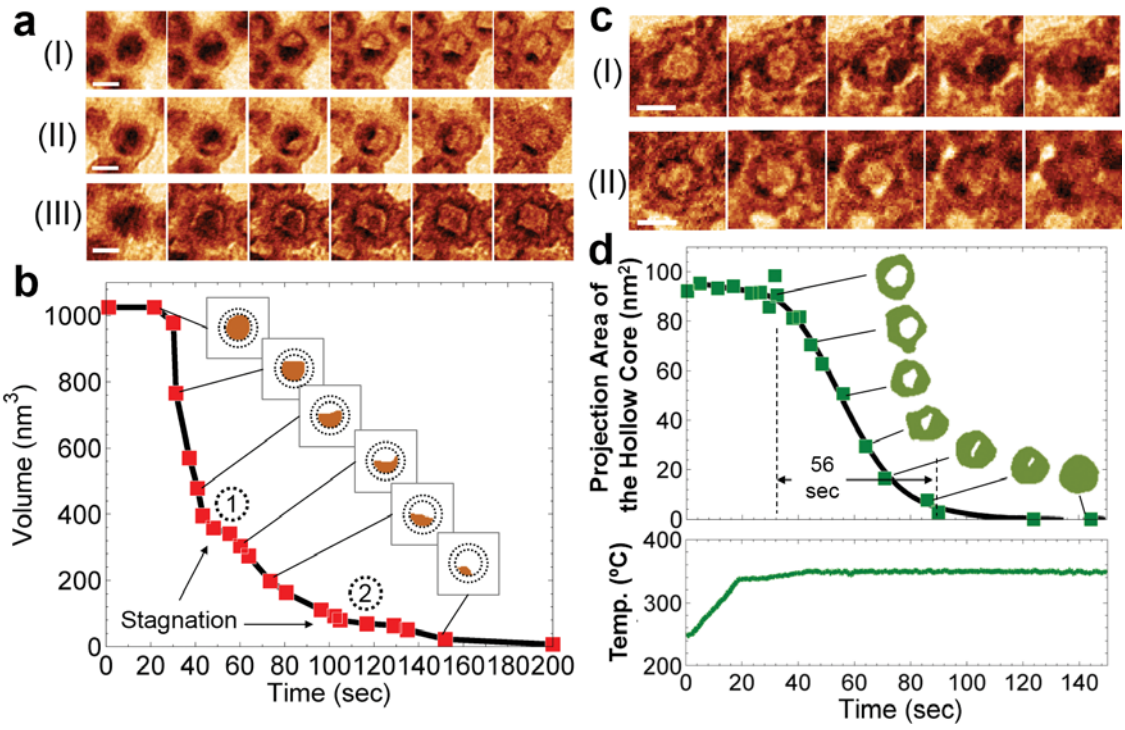

Figure 7. *In situ* heating of cobalt nanoparticles in flowing oxygen. **a**: Real-time reaction dynamics of the Kirkendall effect (Supplementary Movie 1, 150–250°C). **b**: Metallic core volume trajectory of particle I in (**a**). ① and ② mark two diffusion stagnation plateaus. (Simultaneously recorded temperature trajectory is shown in Fig. 6b.) **c**: Restructuring of the hollow oxide structure at 250–350°C in flowing oxygen (Supplementary Movie 2). **d**: Hollow core volume trajectory of particle I in (**c**). Scale bar is 10 nm.

Conclusions

In this article, we have demonstrated a windowed cell gas-flow heating holder that can be used in any conventional TEM and used it to demonstrate real-time observation of an oxidation reaction of cobalt-based nanocatalysts uncovering *in situ* evolution of the Kirkendall effect. The MEMS-type E-cell design allows for a differential pressure as high as 4 bar as well as the preservation of 2 Å fringe resolution at ~1 bar in a 200 keV LaB_6 instrument. The membrane heaters enable heating from 95 to 400°C. The resistivity-based calibration method allows measurement of heating temperatures with ±15°C precision regardless of gas composition and flow conditions. The use of a membrane design for heaters results in a relatively fast heating rate (~5°C/s), a slow drift rate (max <3 nm/s with $\Delta T = 100$°C), and rapid thermal settling (time constant = 75 s with $\Delta T = 100$°C), making it a characterization tool that has several key advantages over other environmental TEM approaches.

Acknowledgments

We performed the *ex situ* TEM experiments at the National Center for Electron Microscopy (NCEM) of the Lawrence Berkeley National Laboratory (LBNL), which is supported by the U.S. Department of Energy (DOE) under Contract # DE-AC02-05CH11231. *In situ* TEM experiments were done using LBNL Materials Sciences Division TEM facilities. We acknowledge support from Bill Smith (Hummingbird Scientific) for development on the temperature measuring method and model. H.L.X. thanks Dr. Sophie Carenco (Salmeron group) and Dr. Selim Alayoglu (Somorjai group) for supplying nanoparticle samples. H.L.X. was supported by Helios SERC of LBNL. H.Z. thanks the support of the DOE Office of Science Early Career Research Program.

References

Accutech Co. (n.d.). Gas/compressible flow calculation notes (FluidFlow3 Design Note 05). Available at http://www.accutech2000.com.au/FluidFlow3/Support/Modelling%20and%20Design%20Notes/Modelling%20and%20Design%20Note%2005%20%20Gas%20Flow.pdf

Allard, L.F., Overbury, S.H., Bigelow, W.C., Katz, M.B., Nackashi, D.P. & Damiano, J. (2012). Novel MEMS-based gas-cell/heating specimen holder provides advanced imaging capabilities for *in situ* reaction studies. *Microsc Microanal* **18**, 656–666.

Atkinson, A. (1986). Diffusion in oxides of the first transition series metals. DTIC Document. Available at www.dtic.mil/dtic/tr/fulltext/u2/a196091.pdf.

Boyes, E.D. & Gai, P.L. (1997). Environmental high resolution electron microscopy and applications to chemical science. *Ultramicroscopy* **67**, 219–232.

Carter, C.B. & Williams, D. (2009). *Transmission Electron Microscopy*. New York: Springer-Verlag.

Chen, W.K., Peterson, N.L. & Reeves, W.T. (1969). Isotope effect for cation self-diffusion in CoO crystals. *Phys Rev* **186**, 887–891.

Chenna, S., Banerjee, R. & Crozier, P.A. (2011). Atomic-scale observation of the Ni activation process for partial oxidation of methane using *in situ* environmental TEM. *Chem Cat Chem* **3**, 1051–1059.

Chuang, W.-H., Luger, T., Fettig, R.K. & Ghodssi, R. (2004). Mechanical property characterization of LPCVD silicon nitride thin films at cryogenic temperatures. *J Microelectromech Sys* **13**, 870–879.

Crane Co. (Ed.). (2011). *Flow of Fluids through Valves, Fittings and Pipe*. Stamford, CT: Crane.

Creemer, J.F., Helveg, S., Hoveling, G.H., Ullmann, S., Molenbroek, A.M., Sarro, P.M. & Zandbergen, H.W. (2008). Atomic-scale electron microscopy at ambient pressure. *Ultramicroscopy* **108**, 993–998.

de Jonge, N., Bigelow, W.C. & Veith, G.M. (2010). Atmospheric pressure scanning transmission electron microscopy. *Nano Lett* **10**, 1028–1031.

de Jonge, N. & Ross, F.M. (2011). Electron microscopy of specimens in liquid. *Nat Nano* **6**, 695–704.

Egerton, R.F. (2011). *Electron Energy-Loss Spectroscopy in the Electron Microscope*, 3rd ed. New York: Springer Science + Business Media.

Frances, M.R. (2010). Controlling nanowire structures through real time growth studies. *Rep Prog Phys* **73**, 114501.

Goldstein, J., Newbury, D.E., Joy, D.C., Lyman, C.E., Echlin, P., Lifshin, E., Sawyer, L. & Michael, J.R. (2003). *Scanning Electron Microscopy and X-Ray Microanalysis*, 3rd ed. New York: Springer.

Gusak, A.M., Zaporozhets, T.V., Tu, K.N. & Gösele, U. (2005). Kinetic analysis of the instability of hollow nanoparticles. *Philos Mag* **85**, 4445–4464.

Haider, M., Müller, H., Uhlemann, S., Zach, J., Loebau, U. & Hoeschen, R. (2008). Prerequisites for a C_c/C_s-corrected ultrahigh-resolution TEM. *Ultramicroscopy* **108**, 167–178.

Hansen, P.L., Wagner, J.B., Helveg, S., Rostrup-Nielsen, J.R., Clausen, B.S. & Topsøe, H. (2002). Atom-resolved imaging of dynamic shape changes in supported copper nanocrystals. *Science* **295**, 2053–2055.

Hansen, T.W. & Wagner, J.B. (2012). Environmental transmission electron microscopy in an aberration-corrected environment. *Microsc Microanal* **18**, 684–690.

Hatty, V., Kahn, H. & Heuer, A.H. (2008). Fracture toughness, fracture strength, and stress corrosion cracking of silicon dioxide thin films. *J Microelectromech Sys* **17**, 943–947.

Jinschek, J.R. & Helveg, S. (2012). Image resolution and sensitivity in an environmental transmission electron microscope. *Micron* **43**, 1156–1168.

Kisielowski, C., Freitag, B., Bischoff, M., van Lin, H., Lazar, S., Knippels, G., Tiemeijer, P., van der Stam, M., von Harrach, S., Stekelenburg, M., Haider, M., Uhlemann, S., Müller, H., Hartel, P., Kabius, B., Miller, D., Petrov, I., Olson, E.A., Donchev, T., Kenik, E.A., Lupini, A.R., Bentley, J., Pennycook, S.J., Anderson, I.M., Minor, A.M., Schmid, A.K., Duden, T., Radmilovic, V., Ramasse, Q.M., Watanabe, M., Erni, R., Stach, E.A., Denes, P. & Dahmen, U. (2008). Detection of single atoms and buried defects in three dimensions by aberration-corrected electron microscope with 0.5-Å information limit. *Microsc Microanal* **14**, 469–477.

Railsback, J.G., Johnston-Peck, A.C., Wang, J. & Tracy, J.B. (2010). Size-dependent nanoscale Kirkendall effect during the oxidation of nickel nanoparticles. *ACS Nano* **4**, 1913–1920.

Reed, S. (1982). The single-scattering model and spatial resolution in X-ray analysis of thin foils. *Ultramicroscopy* **7**, 405–409.

Rez, P. (1983). A transport equation theory of beam spreading in the electron microscope. *Ultramicroscopy* **12**, 29–38.

Sharma, R. (2001). Design and applications of environmental cell transmission electron microscope for *in situ* observations of gas–solid reactions. *Microsc Microanal* **7**, 494–506.

Sharma, R. & Weiss, K. (1998). Development of a TEM to study *in situ* structural and chemical changes at an atomic level during gas-solid interactions at elevated temperatures. *Microsc Res Tech* **42**, 270–280.

Smith, J.M., Van Ness, H.C. & Abbott, M. (2004). *Introduction to Chemical Engineering Thermodynamics*. New York: McGraw-Hill.

Sun, L., Noh, K.W., Wen, J.-G. & Dillon, S.J. (2011). *In situ* transmission electron microscopy observation of silver oxidation in ionized/atomic gas. *Langmuir* **27**, 14201–14206.

Van Aert, S., Chen, J.H. & Van Dyck, D. (2010). Linear versus non-linear structural information limit in high-resolution transmission electron microscopy. *Ultramicroscopy* **110**, 1404–1410.

Vendelbo, S.B., Kooyman, P.J., Creemer, J.F., Morana, B., Mele, L., Dona, P., Nelissen, B.J. & Helveg, S. (2013). Method for local temperature measurement in a nanoreactor for *in situ* high-resolution electron microscopy. *Ultramicroscopy* **133**, 72–79.

Vlassak, J. & Nix, W. (1992). New bulge test technique for the determination of Young's modulus and Poisson's ratio of thin films. *J Mater Res* **7**, 3242–3249.

Yaguchi, T., Suzuki, M., Watabe, A., Nagakubo, Y., Ueda, K. & Kamino, T. (2011). Development of a high temperature-atmospheric pressure environmental cell for high-resolution TEM. *J Electron Microsc* **60**, 217–225.

Yin, Y., Rioux, R.M., Erdonmez, C.K., Hughes, S., Somorjai, G.A. & Alivisatos, A.P. (2004). Formation of hollow nanocrystals through the nanoscale Kirkendall effect. *Science* **304**, 711–714.

Yokosawa, T., Alan, T., Pandraud, G., Dam, B. & Zandbergen, H. (2012). *In-situ* TEM on (de)hydrogenation of Pd at 0.5–4.5 bar hydrogen pressure and 20–400°C. *Ultramicroscopy* **112**, 47–52.

Yoshida, H., Kuwauchi, Y., Jinschek, J.R., Sun, K., Tanaka, S., Kohyama, M., Shimada, S., Haruta, M. & Takeda, S. (2012). Visualizing gas molecules interacting with supported nanoparticulate catalysts at reaction conditions. *Science* **335**, 317–319.